applied sciences

MDPI

Article

Active Vibration Suppression of Stiffened Composite Panels with Piezoelectric Materials under Blast Loads

Chang-Yull Lee [1], **Jin-Young Jung** [2] **and Se-Min Jeong** [3,*]

[1] Department of Aerospace Engineering, Chosun University, Gwangju 61452, Korea; cylee@chosun.ac.kr
[2] National Research Foundation of Korea, Daejeon 34113, Korea; jyjung@nrf.re.kr
[3] Department of Naval Architecture and Ocean Engineering, Chosun University, Gwangju 61452, Korea
* Correspondence: smjeong@chosun.ac.kr; Tel.: +82-62-230-7218

Received: 30 November 2019; Accepted: 26 December 2019; Published: 4 January 2020

Abstract: Transient responses of stiffened panels with piezoelectric sensors and actuators are studied under normal blast loads. The air vehicles could be exposed to blast pulses generated by an explosion or shock-wave disturbances. Thus, active vibration suppression of the vehicles is important under blast loadings. The structural model is designed as a laminated composite panel with lead zirconate titanate (PZT) piezoceramic layers embedded on both top and bottom surfaces. A uniformly distributed blast load is assumed over the whole of the panel surface. The first-order shear deformation theory of plate is adopted, and the extended Hamilton's principle is applied to derive the equations of motions. The numerical model is verified by the comparison with previous data. Using linear quadratic regulator (LQR) control algorithm, vibration characteristics and dynamic responses are compared. As piezoelectric patches are attached on the whole of the surface, the effect of the stiffener's location is studied. Furthermore, the influences of the patch's positions are also investigated through subjection to the blast wave. From various results, in order to get the best control performances, the research aims to find the optimum position of sensor and actuator pairs that is most effective under blast load environments.

Keywords: active vibration control; suppression; stiffener locations; blast loads

---

1. Introduction

Recently, the research relevant to the piezoelectric materials to control the vibration of structures is actively reported in the literature. The applications of the piezoelectric materials are vibration suppression, shape control, active damping, size control, and energy harvesting, etc. The materials can be used as sensors and actuators. At first, direct piezoelectric effect means that the materials generate an electric charge while the model is subjected to a mechanical deformation. Conversely, they could be deformed when some electric charges are applied to structures. This is called the converse piezoelectric effect.

Many engineers have studied composite structures with piezoelectric sensors and actuators. Reddy [1] investigated theoretical formulations and finite element models using the shear deformation plate theories. They analyzed the laminated plates with sensors and actuators under mechanical and electrical loads. Liu et al. [2] presented the active vibration suppression of the laminated composite plates. Lam and Ng [3] also simulated theoretical formulation for the plates with piezoelectric materials. Balamurugan and Narayanan [4] showed the mechanics analysis and performances of piezolaminated plate and shell structures. In addition, Tolliver et al. [5] described the finite element analysis of the piezoelectric transducer. The model of multilayer piezoelectric actuators is derived based on the physical analysis by Zhang et al. [6]. The proposed methods are easy to handle and apply the piezo models. Furthermore, Qian [7] presented the design, optimization, and testing of piezoelectric harvesters for energy scavenging from human walking. Also, Xie et al. [8] designed a self-powered and wireless radio frequency (RF) transmission device using by combination of triboelectric nanogenerator (TENG) and off-the-shelf piezoelectric element.

On the other hand, the dynamic responses of structures under air blast loads have been studied for many years. Luccioni et al. [9] showed the evaluation of pressures and impulses produced by blast loads with the aid of hydrocodes. The numerical and experimental research of a stiffened laminated composite panel under a shock wave was represented by Turkmen and Mecitoglu [10]. Furthermore, Jacinto et al. [11] analyzed numerical responses of metallic panels subjected to explosive loadings.

Recently, research and development of stiffened structures is one of the important subjects in aircraft and aerospace industries. Globally, many engineers have tried to increase the stiffness by using composite stiffened structures in the space launch vehicle. Nowadays, Ma et al. [12,13] studied active vibration control and sound radiation from a rib stiffened panel using velocity feedback method. Also, Liu et al. [14] presented the dynamic analytical solution of piezoelectric stack using piezo-elasticity theory. In addition, Chung et al. [15] studied the dynamic behaviors of stiffened composite model with piezoelectric patches under airflow. The blast loads applied a sharp pressure to the composite structure in a moment.

Though numerous studies on piezoelectric stiffened models have been performed widely up until now, research to suppress the vibrations of stiffened models caused by aerodynamic flows such as blast loads has been studied in a limited range. In other words, many studies have been focused on damages to the structures. Therefore, active vibration suppression of piezoelectric stiffened laminated panels subjected to normal blast waves is studied in this paper. Due to the characteristics of piezoelectric materials as fast responders, the vibration behaviors of stiffened composite panels could be controlled easily by piezoelectric actuators under a blast loading. A stiffened panel with piezoelectric effect is formulated using finite element method. Numerical formulations and results are verified with previous data. Then, vibration behaviors and transient responses are controlled using linear quadratic regulator (LQR) algorithms. Furthermore, numerical results for vibration suppression of stiffened panels under blast load are discussed in detail. The effect of the stiffeners location of the cantilevered model is considered like as general wings of aircrafts. Furthermore, the influences of the piezoelectric patches position also investigated. Consequently, these studies could be easily applied to various types of structures.

2. Stiffened Laminated Panel with Piezoelectric Materials

In aircraft vehicles, there are many skins with an array of stiffening ribs in the wings and fuselage. These structures have been widely used because of their light weight and ability to withstand dynamic loads. In most cases, the catastrophic disaster of the air vehicles was due to the failure of the fuselage under blast loads. The overpressure of the blast loading generated typically acts during few milliseconds. Thus, active vibration control of stiffened composite structures is an important problem. In this regard, a piezo-laminated composite model is designed with stiffeners (shown in Figure 1).

The stiffeners are placed parallel to the geometric coordinates x and y. In this figure, the thickness of the model, the thickness of stiffener, the width of the x-stiffener, and the width of the y-stiffener are t_p, t_{ys}, b_{xs}, and b_{ys}, respectively. The model is a laminated composite structure with lead zirconate titanate (PZT) piezoceramic layers embedded on both top and bottom surfaces to act as a sensor and an actuator, respectively. In addition, the sensor and actuator layers are designed as a single layer.

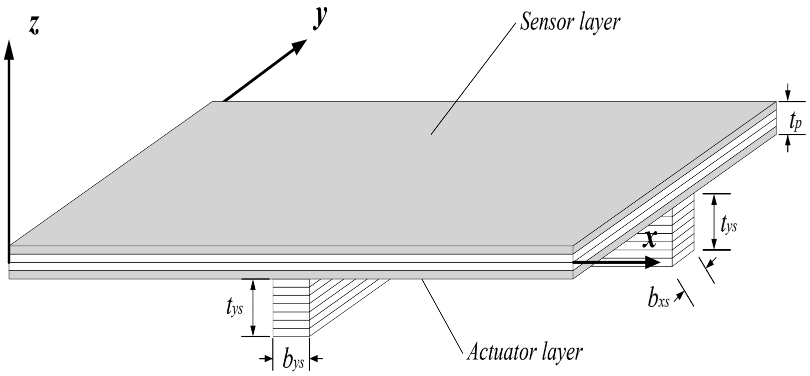

Figure 1. Stiffened model with piezoelectric sensors and actuators.

2.1. Finite Element Formulations

First of all, the k^{th} layer's piezoelectric coupling relations between the elastic and the electrical fields could be presented, and the equations can be written as follows [15]:

$$\mathbf{D}_k = \mathbf{e}_k \boldsymbol{\varepsilon}_k + \boldsymbol{\varepsilon}_k \mathbf{E}_k \tag{1}$$

$$\boldsymbol{\sigma} = \mathbf{Q}\boldsymbol{\varepsilon} - \mathbf{e}_k^T \mathbf{E}_k \tag{2}$$

where $\boldsymbol{\varepsilon}$, $\boldsymbol{\sigma}$, $\mathbf{D}$, and $\mathbf{E}$ are the strain, stress component, electric displacement, and electrical field vectors, respectively. In addition, $\mathbf{e}$, $\boldsymbol{\varepsilon}$, and $\mathbf{Q}$ are piezoelectric constants, permittivity coefficients, and reduced elastic constants matrices, respectively. Equation (1) means the direct piezoelectric effect, and Equation (2) indicates the converse piezoelectric effect.

The stiffened plate elements are derived with the plate element and stiffener elements. The first-order shear deformation theory (FSDT) applied, the displacement fields are defined as follows:

$$\begin{aligned} u(x,y,z) &= u_p^o(x,y) + z\theta_{xp}(x,y), \\ v(x,y,z) &= v_p^o(x,y) + z\theta_{yp}(x,y), \\ w(x,y,z) &= w_p^o(x,y,z). \end{aligned} \tag{3}$$

where u_p^o, v_p^o, and w_p^o are the mid-plane displacements, and θ_{xp} and θ_{yp} are the rotations of transverse normal about x and y, respectively. The displacement fields of the x-directional stiffener and y-directional stiffener are expressed as follows:

$$\begin{aligned} u_{xs}(x,z) &= u_{xs}^o(x) + z\theta_{xs}(x), \;\; w_{xs}(x,z) = w_{xs}^o(x) \\ v_{ys}(y,z) &= v_{ys}^o(y) + z\theta_{ys}(y), \;\; w_{ys}(y,z) = w_{ys}^o(y) \end{aligned} \tag{4}$$

where x-axis is taken along the x-directional stiffener center line and z-axis is its upward normal line. The detailed formulations can be found in reference [16].

The strains are presented as a function of the nodal displacement variables.

$$\begin{aligned} \boldsymbol{\varepsilon}_p &= \left\{ \begin{array}{c} \varepsilon_{xx} \\ \varepsilon_{yy} \\ \gamma_{xy} \end{array} \right\}_p = \left\{ \begin{array}{c} u_{p,x}^o \\ v_{p,y}^o \\ u_{p,y}^o + v_{p,x}^o \end{array} \right\} + z \left\{ \begin{array}{c} \theta_{xp,x} \\ \theta_{yp,y} \\ \theta_{xp,y} + \theta_{yp,x} \end{array} \right\} = \boldsymbol{\varepsilon}_p^o + z\boldsymbol{\kappa}_p = \mathbf{B}_m \boldsymbol{\delta}_p + z\mathbf{B}_b \boldsymbol{\delta}_p \\ \boldsymbol{\gamma}_p &= \left\{ \begin{array}{c} \gamma_{xz} \\ \gamma_{yz} \end{array} \right\}_p = \left\{ \begin{array}{c} w_{p,x}^o - \theta_{p,x} \\ w_{p,y}^o - \theta_{p,y} \end{array} \right\} = \mathbf{B}_s \boldsymbol{\delta}_p \end{aligned} \tag{5}$$

where $\mathbf{B}_m$, $\mathbf{B}_b$, and $\mathbf{B}_s$ are the derivative operators between the strain and nodal displacements.

The stress resultant can be written as

$$\begin{gathered}\mathbf{F} = \mathbf{A}_{ij}\boldsymbol{\varepsilon}_p^o + \mathbf{B}_{ij}\boldsymbol{\kappa}_p - \int_{t_p} \mathbf{e}^T\mathbf{E}dz \\ \mathbf{M} = \mathbf{B}_{ij}\boldsymbol{\varepsilon}_p^o + \mathbf{D}_{ij}\boldsymbol{\kappa}_p - \int_{t_p} z\mathbf{e}^T\mathbf{E}dz \\ \mathbf{V}_p = \mathbf{S}\boldsymbol{\gamma}_p\end{gathered} \tag{6}$$

where $\left(\mathbf{A}_{ij}, \mathbf{B}_{ij}, \mathbf{D}_{ij}\right) = \sum_{k=1}^{n} \int_{z_{k-1}}^{z_k} \mathbf{Q}_{ij}\left(1, z, z^2\right)dz$ and $\mathbf{S}_{ij} = \sum_{k=1}^{n} \kappa_p \int_{z_{k-1}}^{z_k} \mathbf{Q}_{ij}dz$ with $(i, j = 4, 5)$. $\kappa_p = 5/6$ is shear correction factor. $\mathbf{A}_{ij}$, $\mathbf{B}_{ij}$, $\mathbf{D}_{ij}$, and $\mathbf{S}_{ij}$ are extensional stiffness, bending-extension coupling stiffness, bending stiffness, and shear stiffness matrix, respectively.

Then, the electric field vector considering the piezoelectric actuator layers can be derived as follows:

$$\mathbf{E} = \left\{\begin{array}{c} E_x \\ E_y \\ E_z \end{array}\right\} = -\left\{\begin{array}{c} 0 \\ 0 \\ 1/t_a \end{array}\right\}\phi_a = -\mathbf{B}_\phi \phi_a \tag{7}$$

where t_a and ϕ_a are the thickness of the actuator and the electric potential, respectively. The present element has elastic degrees of freedom u_p^o, v_p^o, θ_{xp}, θ_{yp}, and w_p^o per node and electrical degree of freedom ϕ per piezoelectric layer.

On the other hand, the strains of the x-stiffener are indicated as follows [17]:

$$\boldsymbol{\varepsilon}_{xs} = \left\{\begin{array}{c} \varepsilon_{xx} \\ \gamma_{xz} \end{array}\right\}_{xs} = \left[\begin{array}{cccc} 1 & z & 0 & 0 \\ 0 & 0 & 1 & 1 \end{array}\right]\left\{\begin{array}{c} u_{xs,x}^o \\ \theta_{xs,x} \\ \theta_{xs} \\ w_{xs,x}^o \end{array}\right\} = \mathbf{H}_{xs}\boldsymbol{\varepsilon}_{xs}^o \tag{8}$$

The stress resultant can be derived as follows:

$$\left\{\begin{array}{c} F_{xs} \\ M_{xs} \\ V_{xs} \end{array}\right\} = \left[\begin{array}{cccc} A_{xs,11} & B_{xs,11} & 0 & 0 \\ B_{xs,11} & D_{xs,11} & 0 & 0 \\ 0 & 0 & S_{xs,55} & S_{xs,55} \end{array}\right]\boldsymbol{\varepsilon}_{xs}^o = \mathbf{D}_{xs}\boldsymbol{\varepsilon}_{xs}^o \tag{9}$$

where $A_{xs,ij}, B_{xs,ij}, D_{xs,ij}, S_{xs,ij} = \sum_{k=1}^{n} \int_{z_{k-1}}^{z_k} Q_{ij}\left(1,\ z,\ z^2, \kappa_{xs}\right)dz$.

To obtain the energy equations, the strain energy function is derived using the variational principles as follows:

$$\begin{aligned} V^e &= V_p^e + V_{xs}^e \\ &= \tfrac{1}{2}\boldsymbol{\delta}_p^{eT} \int_A \left(\mathbf{B}_m{}^T\mathbf{A}_{ij}\mathbf{B}_m + \mathbf{B}_m{}^T\mathbf{B}_{ij}\mathbf{B}_b + \mathbf{B}_b{}^T\mathbf{B}_{ij}\mathbf{B}_m + \mathbf{B}_b{}^T\mathbf{D}_{ij}\mathbf{B}_b + \mathbf{B}_s{}^T\mathbf{S}_{ij}\mathbf{B}_s\right)dA\boldsymbol{\delta}_p^e \\ &\quad + \tfrac{1}{2}\boldsymbol{\delta}_p^{eT} \int_A \left(\mathbf{B}_m{}^T\mathbf{E}_1\mathbf{B}_\phi + \mathbf{B}_b{}^T\mathbf{E}_2\mathbf{B}_\phi\right)dA\phi^e + \tfrac{1}{2}\boldsymbol{\delta}_p^{eT} \int_L \mathbf{T}_{xs}{}^T\mathbf{B}_{xs}{}^T\mathbf{D}_{xs}\mathbf{B}_{xs}\mathbf{T}_{xs}dx\boldsymbol{\delta}_p^e \\ &= \tfrac{1}{2}\boldsymbol{\delta}_p^{eT}\mathbf{K}_p^e\boldsymbol{\delta}_p^e + \tfrac{1}{2}\boldsymbol{\delta}_p^{eT}\mathbf{K}_{u\phi}^e\phi^e + \tfrac{1}{2}\boldsymbol{\delta}_p^{eT}\mathbf{K}_{xs}^e\boldsymbol{\delta}_p^e \end{aligned} \tag{10}$$

where $\mathbf{E}_1, \mathbf{E}_2 = \int_{z_p} \mathbf{e}_{ij}{}^T(1, z)dz$, $\mathbf{D}_{xs} = b_{xs}\int_{t_{xs}} \mathbf{H}_{xs}{}^T\mathbf{Q}_{xs}\mathbf{H}_{xs}dz$. $\mathbf{K}_p^e$ is the element stiffness matrix of plate and $\mathbf{K}_{u\phi}^e$ is the element elastic-electric coupling stiffness matrix. $\mathbf{K}_{xs}^e$ is the element stiffness matrix of the x-stiffeners.

The element kinetic energy can be written as

$$\begin{aligned} T^e &= T_p^e + T_{xs}^e \\ &= \tfrac{1}{2}\dot{\boldsymbol{\delta}}_p^{eT} \int_A \left[P\left(\overline{\mathbf{N}}_{pu}{}^T\overline{\mathbf{N}}_{pu} + \overline{\mathbf{N}}_{pv}{}^T\overline{\mathbf{N}}_{pv} + \overline{\mathbf{N}}_{pw}{}^T\overline{\mathbf{N}}_{pw}\right) + I\left(\overline{\mathbf{N}}_{p\theta_x}{}^T\overline{\mathbf{N}}_{p\theta_x} + \overline{\mathbf{N}}_{p\theta_y}{}^T\overline{\mathbf{N}}_{p\theta_y}\right)\right]dA\dot{\boldsymbol{\delta}}_p^e \\ &\quad + \tfrac{1}{2}\dot{\boldsymbol{\delta}}_p^{eT}\mathbf{T}_{xs}{}^T \int_L b\left[P\left(\overline{\mathbf{N}}_{xsu}{}^T\overline{\mathbf{N}}_{xsu} + \overline{\mathbf{N}}_{xsw}{}^T\overline{\mathbf{N}}_{xsw}\right) + I\overline{\mathbf{N}}_{xs\theta_x}{}^T\overline{\mathbf{N}}_{xs\theta_x}\right]dx\mathbf{T}_{xs}\dot{\boldsymbol{\delta}}_p^e \\ &= \tfrac{1}{2}\dot{\boldsymbol{\delta}}_p^{eT}\mathbf{M}_p^e\dot{\boldsymbol{\delta}}_p^e + \tfrac{1}{2}\dot{\boldsymbol{\delta}}_p^{eT}\mathbf{M}_{xs}^e\dot{\boldsymbol{\delta}}_p^e \end{aligned} \tag{11}$$

where $P, I = \sum_{k=1}^{n} \int_{z_{k-1}}^{z_k} \rho\left(1, z^2\right) dz$ and $\overline{\mathbf{N}}$ is the shape function matrices relating the primary variables.

$\mathbf{M}_p^e$ is the element mass matrix of plate and $\mathbf{M}_{xs}^e$ is the element mass matrix of the stiffeners.

The element electrical energy is calculated as follows:

$$\begin{aligned} W_E^e &= \tfrac{1}{2}\int_{V_p} \mathbf{E}^T\left(\mathbf{e}\boldsymbol{\varepsilon}_p + \boldsymbol{\varepsilon}\mathbf{E}\right)dV \\ &= -\tfrac{1}{2}\phi^{eT}\int_A\left({\mathbf{B}_\phi}^T\mathbf{E}_1\mathbf{B}_m + {\mathbf{B}_\phi}^T\mathbf{E}_2\mathbf{B}_b\right)dA\boldsymbol{\delta}_p^e + \tfrac{1}{2}\phi^{eT}\int_A {\mathbf{B}_\phi}^T\mathbf{E}_3\mathbf{B}_\phi dA\phi^e \\ &= -\tfrac{1}{2}\phi^{eT}\mathbf{K}_{\phi u}\boldsymbol{\delta}_p^e + \tfrac{1}{2}\phi^{eT}\mathbf{K}_{\phi\phi}\phi^e \end{aligned} \tag{12}$$

where $\mathbf{K}_{\phi u}$ is element elastic-electric coupling stiffness matrix and $\mathbf{K}_{\phi\phi}$ is element electric stiffness matrix. $\mathbf{E}_3 = \int_{z_p} \boldsymbol{\varepsilon}_{ij} dz$ and V_p is the volume of the piezoelectric layer.

The virtual work and the applied electrical charge density are derived as follows:

$$\begin{aligned} \Delta W_S^e &= \Delta\boldsymbol{\delta}_p^e\int_{S_1} {\mathbf{B}_f}^T\mathbf{f}_s dA - \Delta\phi^{eT}\int_{S_2} {\mathbf{B}_\phi}^T\mathbf{q}_s dA \\ &= \Delta\boldsymbol{\delta}_p^e\mathbf{F}_s^e + \Delta\phi^{eT}\mathbf{F}_q^e \end{aligned} \tag{13}$$

where S_1 and S_2 are the surface areas that the surface forces and electrical charges are applied, respectively. $\mathbf{F}_s^e$ is the applied mechanical force due to surface forces, and $\mathbf{F}_q^e$ is the applied electrical charge.

The governing equation can be described using the Hamilton's principle.

$$\mathbf{M}_{uu}^e\ddot{\boldsymbol{\delta}}_p^e + \mathbf{K}_{uu}^e\boldsymbol{\delta}_p^e + \mathbf{K}_{u\phi}^e\phi^e = \mathbf{F}_s^e \tag{14}$$

$$\mathbf{K}_{\phi u}^e\boldsymbol{\delta}_p^e + \mathbf{K}_{\phi\phi}^e\phi^e = \mathbf{F}_q^e \tag{15}$$

where $\mathbf{M}_{uu}^e = \mathbf{M}_p^e + \mathbf{M}_{xs}^e$, $\mathbf{K}_{uu}^e = \mathbf{K}_p^e + \mathbf{K}_{xs}^e$.

Then, the global dynamic equation is obtained as follows:

$$\mathbf{M}_{uu}\ddot{\boldsymbol{\delta}}_p + \mathbf{C}_{uu}\dot{\boldsymbol{\delta}}_p + \left(\mathbf{K}_{uu} + \mathbf{K}_{u\phi}{\mathbf{K}_{\phi\phi}}^{-1}\mathbf{K}_{\phi u}\right)\boldsymbol{\delta}_p = \mathbf{F}_s + \mathbf{K}_{u\phi}\phi_a \tag{16}$$

where damping matrix $\mathbf{C}_{uu}$ is assumed as $\mathbf{C}_{uu} = \alpha\mathbf{M}_{uu} + \beta\mathbf{K}_{uu}$.

Next, modal transformations and state-space formulations are derived. The nodal displacement is represented by

$$\boldsymbol{\delta}_p = \boldsymbol{\Phi}\boldsymbol{\eta} \tag{17}$$

The global dynamic equation can be transformed to the reduced modal space form as follows:

$$\boldsymbol{\Phi}^T\mathbf{M}_{uu}\boldsymbol{\Phi}\boldsymbol{\eta} + \boldsymbol{\Phi}^T\mathbf{C}_{uu}\boldsymbol{\Phi}\dot{\boldsymbol{\eta}} + \boldsymbol{\Phi}^T\left(\mathbf{K}_{uu} + \mathbf{K}_{u\phi}{\mathbf{K}_{\phi\phi}}^{-1}\mathbf{K}_{\phi u}\right)\boldsymbol{\Phi}\boldsymbol{\eta} = \boldsymbol{\Phi}^T\mathbf{F}_s + \boldsymbol{\Phi}^T\mathbf{K}_{u\phi}\phi_a \tag{18}$$

$$\overline{\mathbf{M}}\ddot{\boldsymbol{\eta}} + \overline{\mathbf{C}}\dot{\boldsymbol{\eta}} + \overline{\mathbf{K}}\boldsymbol{\eta} = \overline{\mathbf{F}}_s + \overline{\mathbf{K}}_{u\phi}\phi_a \tag{19}$$

Introducing the state-space variable $\boldsymbol{\xi} = \left\{ \begin{matrix} \boldsymbol{\eta} & \dot{\boldsymbol{\eta}} \end{matrix} \right\}^T$, state-space form of the global dynamic equation is given by

$$\dot{\boldsymbol{\xi}} = \mathbf{A}_{st}\boldsymbol{\xi} + \mathbf{B}_{st}\phi_a + \mathbf{U}_f \tag{20}$$

where ϕ_a is the control input and some valuables are defined as follows:

$$\mathbf{A}_{st} = \begin{bmatrix} 0 & \mathbf{I} \\ -\overline{\mathbf{M}}^{-1}\overline{\mathbf{K}} & -\overline{\mathbf{M}}^{-1}\overline{\mathbf{C}} \end{bmatrix}, \mathbf{B}_{st} = \left\{ \begin{matrix} 0 \\ \overline{\mathbf{M}}^{-1}\overline{\mathbf{K}}_{u\phi} \end{matrix} \right\}, \mathbf{U}_f = \left\{ \begin{matrix} 0 \\ \overline{\mathbf{M}}^{-1}\overline{\mathbf{F}}_s \end{matrix} \right\} \tag{21}$$

The output equations can be written in the physical coordinates and state space coordinates as

$$\mathbf{y} = \mathbf{C}_o \boldsymbol{\delta}_p, \overline{\mathbf{y}} = \begin{Bmatrix} \mathbf{C}_o \boldsymbol{\Phi} \\ 0 \end{Bmatrix} \boldsymbol{\xi} = \overline{\mathbf{C}}_o \boldsymbol{\xi} \tag{22}$$

where $\mathbf{C}_o$ is the output matrix.

Finally, the linear quadratic regulator (LQR) control algorithm [4,18] is applied. The control gain can be obtained.

$$J = \frac{1}{2} \int_0^\infty \left(\boldsymbol{\xi}^T \mathbf{Q} \boldsymbol{\xi} + {\phi_a}^T \mathbf{R} \phi_a \right) dt \tag{23}$$

where $\mathbf{R}$ and $\mathbf{Q}$ are positive definite weighting matrices and semi-positive definite, respectively. The actuating voltage can be derived as follows:

$$\phi_a(t) = -\mathbf{G}_c \boldsymbol{\xi} = -\mathbf{R}^{-1} {\mathbf{B}_{st}}^T \mathbf{P} \boldsymbol{\xi} \tag{24}$$

Which is determined by the constant solution $\mathbf{P}$ of the Riccati equation.

$${\mathbf{A}_{st}}^T \mathbf{P} + \mathbf{P} \mathbf{A}_{st} - \mathbf{P} \mathbf{B}_{st} \mathbf{R}^{-1} {\mathbf{B}_{st}}^T \mathbf{P} + \mathbf{Q} = 0 \tag{25}$$

2.2. Blast Loads

The air vehicles could be exposed to blast pulses generated by an explosion or shock-wave disturbances. Figure 2 presents the expected form of an ideal blast wave. It is increased at the shock front by an abrupt pressure. A negative phase follows, and oscillations quickly die away. These oscillations are not dominant compared with the first positive phase. The pressure is also assumed to be distributed over the whole of the surface. The total pressure is defined by Friedländer decay function [19] as follows:

$$P(t)_{blast} = p_m \left(1 - \frac{t}{t_p} \right) e^{-a' t / t_p} \tag{26}$$

where p_m, t_p, and a' are peak pressure, positive phase duration, and the waveform parameter, respectively. The parameters of the Friedländer decay equation are chosen as p_m = 28.9 kPa, t_p = 1.8 ms, and $a' = 0.35$ [10].

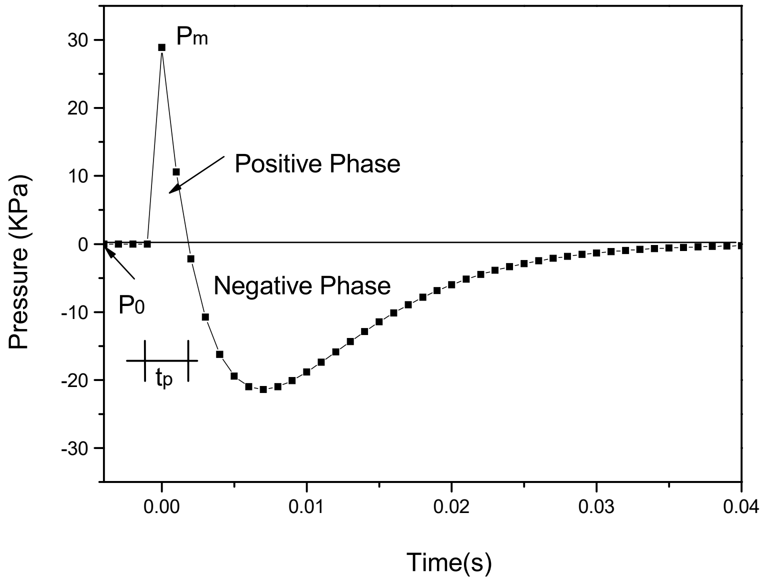

Figure 2. Variations of blast loading according to time [20].

3. Numerical Results and Discussions

3.1. Code Verifications

To verify the accuracy of the present numerical results, three cases are compared with the previous data in the literature. The first case is the cantilevered composite model with the upper and lower surfaces by piezoelectric ceramics. The plates have four composite layers $[-45/45/-45/45]$. The total thickness of the composite model is 1 mm and each layer has the same thickness of 0.25 mm. The two outer piezoelectric layers are of 0.1 mm thickness. In addition, the adhesive layers are neglected. The panel consists of T300/976 graphite-epoxy composites, and the piezoelectric material is PZT F1195N, as presented in Table 1 [21]. The centerline deflections of the composite model with various input voltages are presented in Figure 3. The results are in good agreement with the data obtained by Lam et al. [21].

Table 1. Material properties [21].

Properties	PZT Piezoceramic	T300/976
Young's modulus (GPa): E_{11}	63.0	150
$E_{22} = E_{33}$	63.0	9.0
Poisson's ratio: $\nu_{12} = \nu_{13}$	0.3	0.3
ν_{23}	0.3	0.3
Shear modulus (GPa): $G_{12} = G_{13}$	24.2	7.10
G_{23}	24.2	2.50
Density (kg/m^3): ρ	7600	1600
Piezoelectric constants (m/V): $d_{31} = d_{32}$	254×10^{-12}	-
Electrical permittivity (F/m): $\epsilon_{11}=\epsilon_{22}$	15.3×10^{-9}	-
ϵ_{33}	15.0×10^{-9}	-

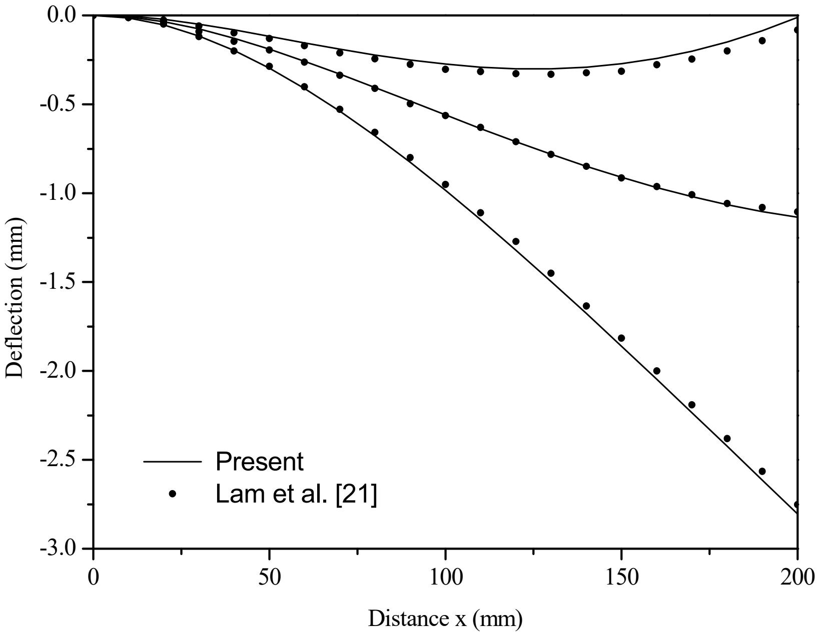

Figure 3. The centerline deflections with various input voltages.

Secondly, the deflection responses of the model under blast loads. The material properties of E, ν, and ρ are 206.84 GPa, 0.3, and 7900 kg/m^3, respectively. The dynamic response is calculated using mode superposition method, and time step is 0.05 ms. Figure 4 shows the deflection history at the center of the model. The present results are almost same with the previous works by Sheikh et al. [22].

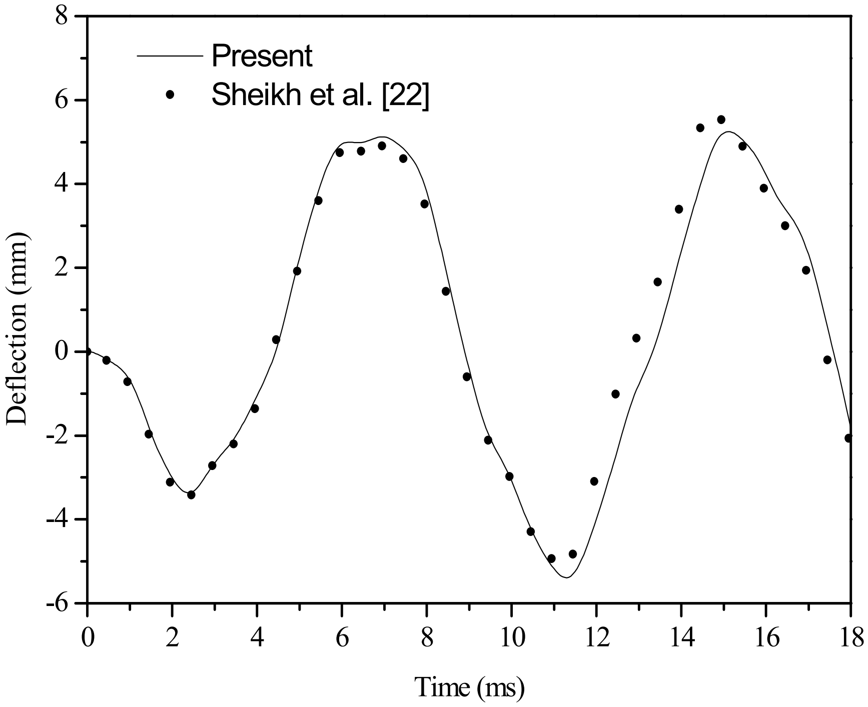

Figure 4. Displacement-time responses of the center of the square model subjected to air blast.

The last case is the polyester model with stiffeners placed at the center. Two opposite edges are free, and the others are clamped. The structure and stiffeners are made with the isotropic materials as follows: E = 7.0 GPa, G = 2.6 GPa, ρ = 1504.2 kg/m^3 and ν = 0.345. The natural frequencies of the model are well-matched with the previous data [16,23], as shown in Table 2.

Table 2. Natural frequencies of stiffened models.

Natural Frequency (Hz)	Ref. [16]	Ref. [23]	Present
1st	68.61	68.47	68.13
2nd	71.20	68.66	68.77
3rd	124.70	119.59	117.55
4th	150.40	162.16	160.128
5th	183.20	177.11	177.45
6th	184.80	177.39	178.31

3.2. The Evaluation of Stiffeners' Locations

Figure 5 shows the cantilevered laminated composite panel with two x-stiffeners. Piezoelectric ceramics are boded at the upper and lower surfaces of the structure. The material properties of the composite panel (T300/976 graphite-epoxy) and the piezoceramic (PZT G1195N) are already presented in Table 1. The structural model is consist of four layers $(15^\circ/-15^\circ/-15^\circ/15^\circ)$ with (0.4/0.4/0.4/0.4) mm layers. The stiffeners with width 6 mm and depth 12 mm are made of the same materials. The thickness of each piezoceramic layer is 0.2 mm.

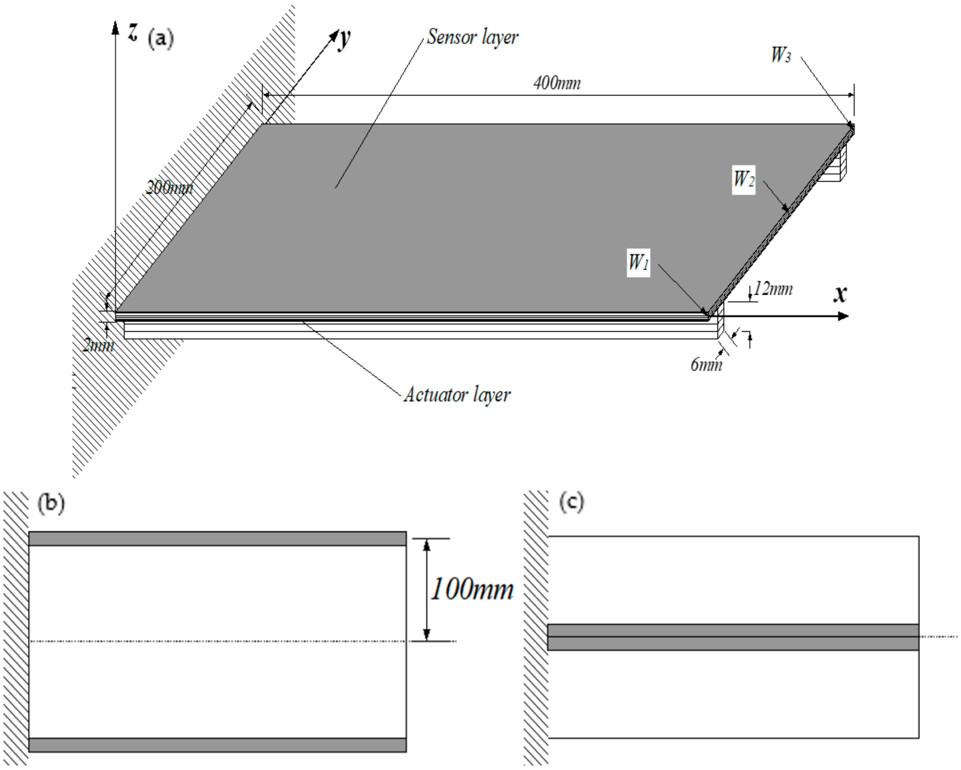

Figure 5. Cantilevered piezoelectric composite model and two cases of the stiffener's location: (**a**) Stiffened composite model; (**b**) Stiffener Case 1; (**c**) Stiffener Case 2.

As mentioned in advance, the upper piezo layer acts as a sensor and the lower layer is assumed as an actuator. Jacinto et al. [11] investigated the experimental and computational analysis of a panel under blast loads, and the data are used in this research. The LQR optimal control algorithm is adopted to the structure. Modal superposition method is applied to the analysis. In addition, the initial damping ratio is assumed to be 0.7%. The transient responses are calculated with the Newmark-direct integration method.

At first, the effect of the stiffener's location on the suppression of the model is studied. The two kinds of cases are presented in Figure 5b,c. The stiffeners are placed at both end sides in Case 1, while the stiffeners are located in the middle part in Case 2. Then, the first six natural frequencies of the stiffened panel with different stiffener location listed in Table 3. It can be seen from Table 3 that the natural frequencies of the Stiffener Case 1 are higher than that of the Stiffener Case 2. This means that the stiffened panel in Case 1 is stiffer than Case 2.

Table 3. Natural frequencies of different stiffener cases.

Natural Frequency (Hz)	Stiffener Case 1	Stiffener Case 2
1st	67.6098	39.6451
2nd	117.7273	78.6680
3rd	155.3218	133.6110
4th	212.1017	178.2795
5th	290.4140	214.3758
6th	379.4205	273.2984

Figure 6 shows magnitude-frequency responses for the two cases of stiffened panel using LQR method. The weighting matrices **Q** and **R** are as follows:

$$\mathbf{Q} = \frac{1}{7\times10^{35}}\begin{bmatrix} \boldsymbol{\Omega}^2 & 0 \\ 0 & \mathbf{I} \end{bmatrix},\ \mathbf{R} = 1\times10^{-2} \text{ and } 1\times10^{-3} \tag{27}$$

where $\boldsymbol{\Omega}^2$ is a diagonal matrix that stores the squares of the natural frequencies ω_i^2 and **I** is the unit matrix with suitable size. When the location of the stiffeners is centered (Case 2), the magnitude of the model is the higher than in the other case (Case 1). In addition, the peak point appeared earlier than Case 1.

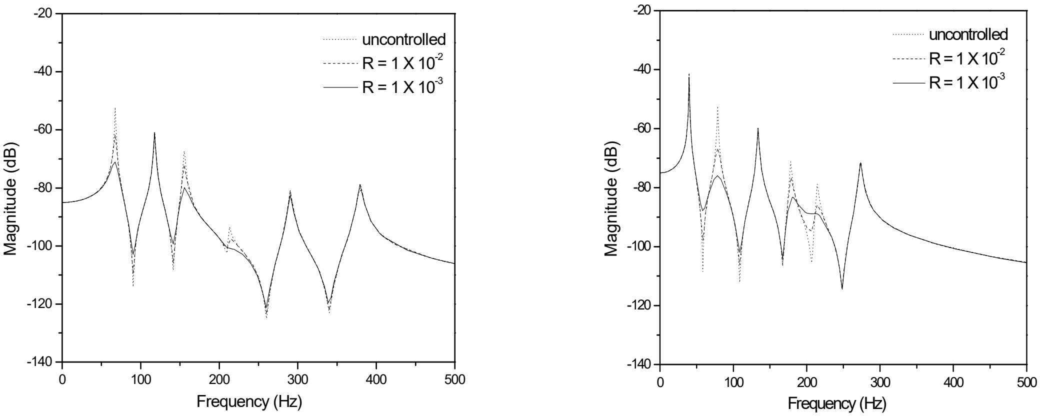

(**a**) (**b**)

Figure 6. Magnitude-frequency responses with two locations of stiffeners using linear quadratic regulator (LQR) control: (**a**) Stiffener Case 1; (**b**) Stiffener Case 2.

Figure 7 describes phase-frequency responses for the two cases of stiffened panel using LQR method. The results represent that controlled responses have the lower magnitude of the first, second, and third bending modes. When the stiffened panel is under uniformly distributed blast pressures, the vertical displacement (W_2) at the tip (0.4, 0.1 m), the transverse bending and the lateral twisting for various **R** are given in Figures 8–10. The transverse bending (W_T) and the lateral twisting (W_R) are defined as in Ref. [4], and the equations are as follows:

$$W_T = \frac{W_2 - (W_1 + W_3)/2}{C},\ W_R = \frac{W_1 - W_3}{C} \tag{28}$$

where W_1, W_2, and W_3 are the vertical deflections at locations already shown in Figure 5a.

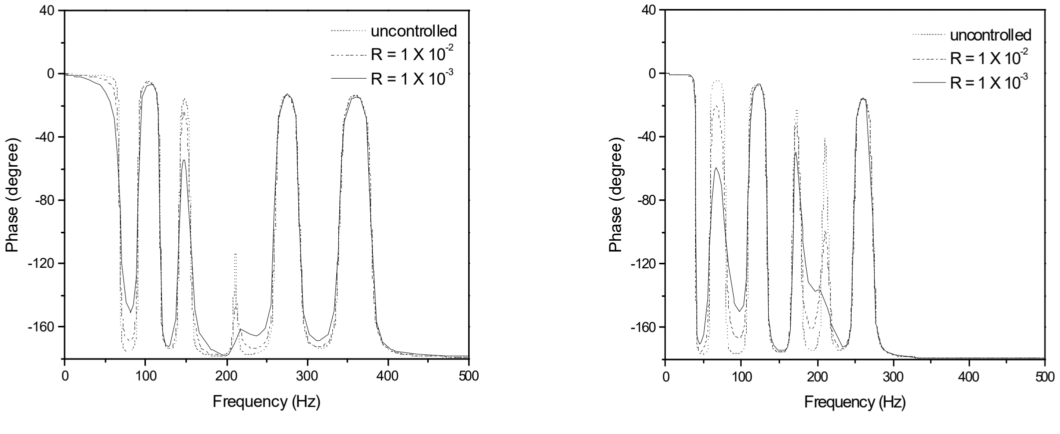

(**a**) (**b**)

Figure 7. Phase-frequency responses with two locations of stiffener using LQR control: (**a**) Stiffener Case 1; (**b**) Stiffener Case 2.

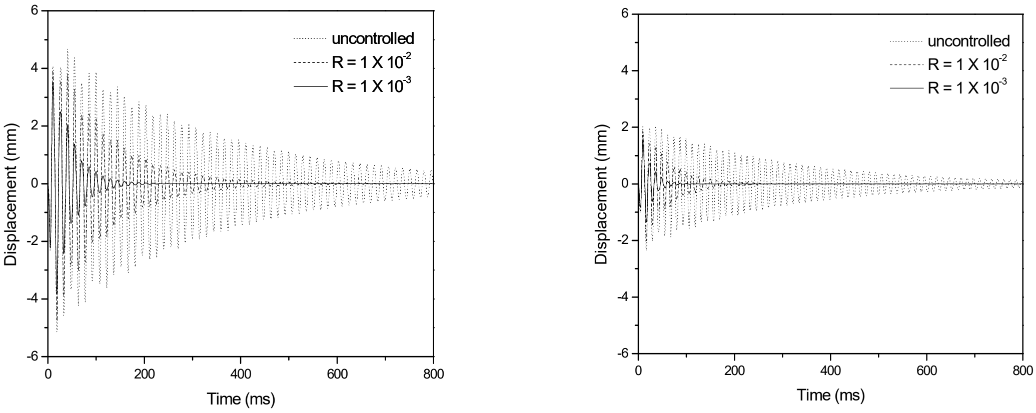

(**a**) (**b**)

Figure 8. Vertical displacement responses with two locations of stiffener using LQR control: (**a**) Stiffener Case 1; (**b**) Stiffener Case 2.

Figure 8 represents vertical displacement responses with two locations of stiffener using LQR control method. The vertical displacement is initially high in Case 1, however the displacement quickly decreased according to time. This is due to the increased stiffness with stiffeners location. On the other hand, both cases showed effective responses to the LQR controller. In other words, it can be seen that the piezoelectric actuator works effectively.

Figure 9 shows transverse bending responses with two locations of stiffener using the LQR control method. The results of the Stiffener Cases 1 and 2 show a similar tendency of vertical displacement in Figure 8. The transverse bending is also initially high in Case 1, however the bending quickly decreased according to time. The vibration oscillations are damped out more quickly with higher control parameters.

Figure 10 shows lateral twisting responses with two locations of stiffeners using the LQR control method. Unlike the previous results in Figures 8 and 9, the lateral twisting was of higher initial value in Case 2. Overall, it could be mentioned that the bending modes can be controlled effectively by the piezoelectric actuators, but the control of torsion is weak for two stiffener cases.

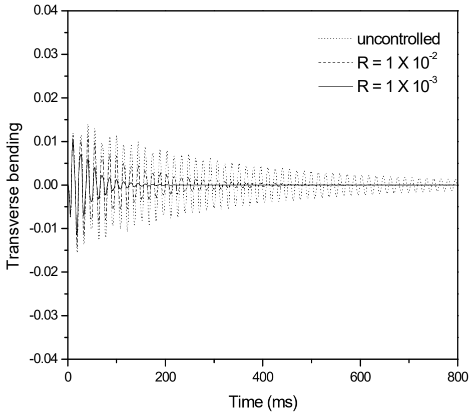

(**a**)

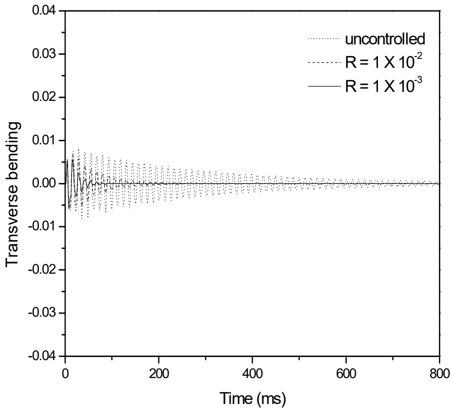

(**b**)

Figure 9. Transverse bending responses with two locations of stiffener using LQR control: (**a**) Stiffener Case 1; (**b**) Stiffener Case 2.

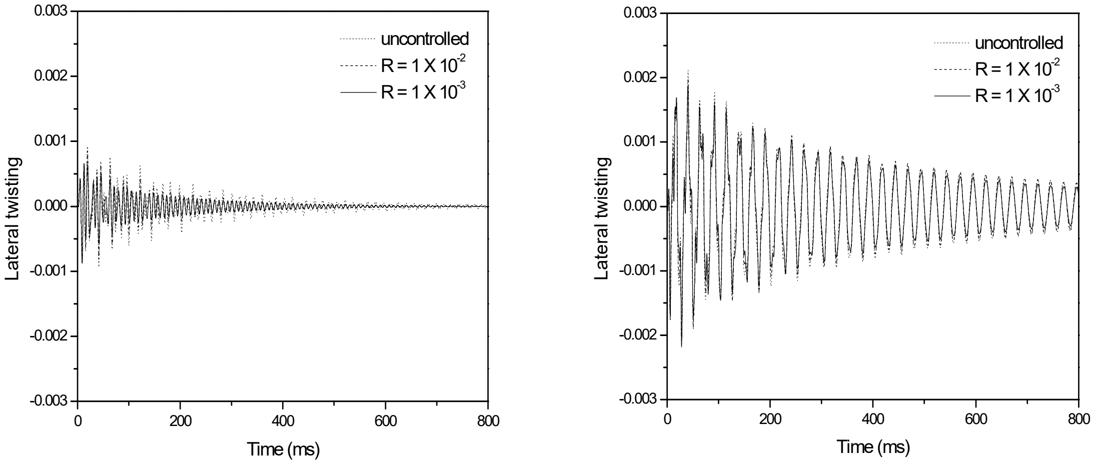

(**a**) (**b**)

Figure 10. Lateral twisting responses with two locations of stiffener using LQR control: (**a**) Stiffener Case 1; (**b**) Stiffener Case 2.

3.3. Evaluation of Positions for Piezoelectric Patches

The effect of positions is studied for the piezoelectric patches on the transient behaviors of the stiffened model under blast load. To investigate the effect of sensors and actuators locations on the control performances, the stiffened model is performed for two different positions of piezoelectric pairs that are attached on top and bottom surfaces, as shown in Figure 11. Each model has eight piezoelectric patches, and the dimensions of each sensor and actuator patch are 0.05 m × 0.05 m. The center points of the Models I and II are 0.05 m and 0.35 m away from the clamped edge, respectively. To investigate the control effects, two parameters are chosen. One parameter is settling time that oscillation does not exceed the limit value of each transient responses. The limit values of the vertical displacement, the transverse bending, and the lateral twisting are 0.4 mm, 0.002, and 0.002, respectively. For other parameter, the limit is the maximum response of the models.

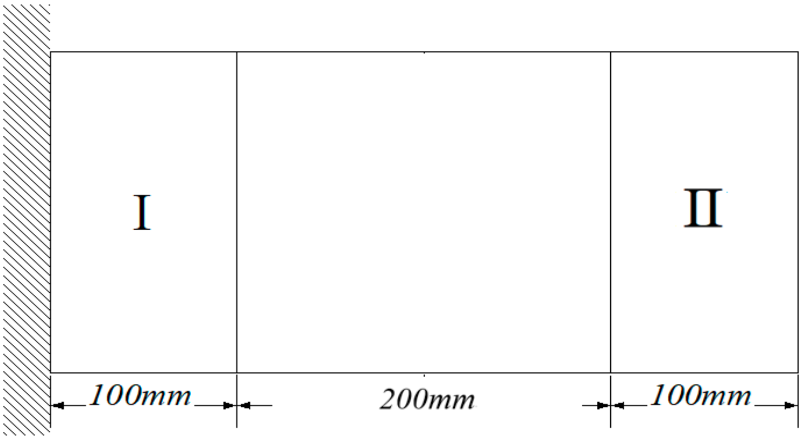

Figure 11. Two models of piezoelectric patch position.

Table 4 shows that the settling time of the two models is obtained using the LQR control algorithm under uniformly distributed blast loads. The models I and II with Stiffener Case 1 have longer settling time than that of the others in the vertical displacement and the transverse bending. The vertical displacement and the transverse bending of the stiffener's location at Stiffener Case 2 is damped out more quickly for the Model I and II. Also, lateral twisting closed to the free end is damped out more quickly.

Table 4. Settling time of two models for LQR control.

	Stiffener Location	**Model I**	**Model II**
Vertical displacement (s)	case 1	0.2848	0.2204
	case 2	0.1139	0.1844
Transverse bending (s)	case 1	0.2857	0.1883
	case 2	0.2569	0.1910
Lateral twisting (s)	case 1	0.2027	0.0592
	case 2	1.0472	0.3362

Table 5 presents the comparison of maximum responses. These results indicate that Model II has the lower peak response for many cases of stiffeners' locations. From Tables 4 and 5, different control performance results are obtained in various positions of piezoelectric pairs. It is important to obtain the optimal design with maximum control effect.

Table 5. Maximum responses of two models for LQR control.

	Stiffener Location	**Model I**	**Model II**
Maximum vertical displacement (mm)	case 1	8.0696	5.6853
	case 2	1.8378	2.6561
Maximum transverse bending (mm)	case 1	0.0359	0.0183
	case 2	0.0453	0.0127
Maximum lateral twisting (mm)	case 1	0.0070	0.0035
	case 2	0.0195	0.0056

4. Conclusions

This paper presents vibration suppression control of a stiffened model with piezoelectric sensors and actuators under blast loads. The air vehicles could be exposed to blast pulses generated by an explosion or shock-wave disturbances. The blast wave is assumed to be uniformly distributed on the panel surface. The linear quadratic regulator (LQR) method is chosen as a control algorithm. As piezoelectric patches are distributed on the whole surfaces of the model, the effect of stiffener's location is investigated. Furthermore, the effect of piezoelectric patches position is also studied on the transient responses of the stiffened structure under blast load. The most effective position of patches can be determined with settling time and maximum responses. Consequently, this presented analysis could be easily applied to various types of models. In order to get the best control performances, the research aimed to find the optimum position of sensor and actuator pairs that is most effective under blast load environments.

Author Contributions: C.-Y.L. participated in the design, computational analysis and writing. J.-Y.J. played an important role in initial overall research. S.-M.J. participated in the supervision of analysis and paper. All authors have read and agreed to the published version of the manuscript.

Funding: This research received no external funding.

Conflicts of Interest: The authors declare no conflict of interest.

References

1. Reddy, J.N. On laminated composite plates with integrated sensors and actuators. *Eng. Struct.* **1999**, *21*, 569–593. [CrossRef]
2. Liu, G.R.; Peng, X.Q.; Lam, K.Y.; Tani, J. Vibration control simulation of laminated composite plates with integrated piezoelectrics. *J. Sound Vibr.* **1999**, *220*, 827–846. [CrossRef]
3. Lam, K.Y.; Ng, T.Y. Active control of composite plates with integrated piezoelectric sensors and actuators under various dynamic loading conditions. *Smart Mater. Struct.* **1999**, *8*, 223–237. [CrossRef]
4. Balamurugan, V.; Narayanan, S. Shell finite element for smart piezoelectric composite plate/shell structures and its application to the study of active vibration control. *Finite Elem. Anal. Des.* **2001**, *37*, 713–738. [CrossRef]
5. Tolliver, L.; Xu, T.B.; Jiang, X. Finite element analysis of the piezoelectric stacked-hybats transducer. *Smart Mater. Struct.* **2013**, *22*, 035015. [CrossRef]
6. Zhang, Y.K.; Lu, T.F.; Al-Sarawi, S. Formulation of a simple distributed-parameter model of multilayer piezoelectric actuators. *J. Intell. Mater. Syst. Struct.* **2016**, *27*, 1485–1491. [CrossRef]
7. Qian, F.; Xu, T.B.; Zuo, L. Design, optimization, modeling and testing of a piezoelectric footwear energy harvester. *Energy Convers. Manag.* **2018**, *171*, 1352–1364. [CrossRef]
8. Xie, Y.; Long, J.; Zhao, P.; Chen, J.; Luo, J.; Zhang, Z.; Li, K.; Han, Y.; Hao, X.; Qu, Z.; et al. A self-powered radio frequency (RF) transmission system based on the combination of triboelectric nanogenerator (TENG) and piezoelectric element for disaster rescue/relief. *Nano Energy* **2018**, *54*, 331–340. [CrossRef]
9. Luccioni, B.; Ambrosini, R.D.; Danesi, R. Blast load assessment using hydrocodes. *Eng. Struct.* **2006**, *28*, 1736–1744. [CrossRef]
10. Turkmen, H.S.; Mecitoglu, Z. Dynamic response of a stiffened laminated composite plate subjected to blast load. *J. Sound Vibr.* **1999**, *221*, 371–389. [CrossRef]
11. Jacinto, A.C.; Ambrosini, R.K.; Danesi, R.F. Experimental and computational analysis of plates under air blast loading. *Int. J. Impact Eng.* **2001**, *25*, 927–947. [CrossRef]
12. Ma, X.; Wang, L.; Xu, J. Active Vibration control of rib stiffened plate by using decentralized velocity feedback controllers with inertial actuators. *Appl. Sci.* **2019**, *9*, 3188. [CrossRef]
13. Ma, X.; Chen, K.; Xu, J. Active control of sound transmission through orthogonally rib stiffened double-panel structure: Mechanism analysis. *Appl. Sci.* **2019**, *9*, 3286. [CrossRef]
14. Liu, X.; Wang, J.; Li, W. Dynamic analytical solution of a piezoelectric stack utilized in an actuator and a generator. *Appl. Sci.* **2018**, *8*, 1779. [CrossRef]
15. Chung, N.T.; Thuy, N.N.; Thu, D.T.N.; Chau, L.H. Numerical and experimental analysis of the dynamic behavior of piezoelectric stiffened composite plates subjected to airflow. *Math. Probl. Eng.* **2019**, *2019*, 10. [CrossRef]
16. Attaf, B.; Hollaway, L. Vibration analyses of stiffened and unstiffened composite plates subjected to in-plane loads. *Composites* **1990**, *21*, 117–126. [CrossRef]

17. Sadek, E.A.; Tawfik, S.A. A finite element model for the analysis of stiffened laminated plates. *Comput. Struct.* **2000**, *75*, 369–383. [CrossRef]
18. Kumar, E.V.; Raaja, G.S.; Jerome, J. Adaptive PSO for optimal LQR tracking control of 2 DoF laboratory helicopter. *Appl. Soft. Comput.* **2016**, *41*, 77–90. [CrossRef]
19. Gupta, A.D.; Gregory, F.H.; Bitting, R.L.; Bhattacharya, S. Dynamic analysis of an explosively loaded hinged rectangular plate. *Comput. Struct.* **1987**, *26*, 339–344. [CrossRef]
20. Hetherington, J.G.; Smith, P.D. *Blast and Ballistic Loading of Structures*; Butterworth-Heinemann Ltd.: London, UK, 1994; pp. 30–57.
21. Lam, K.Y.; Peng, X.Q.; Liu, G.R.; Reddy, J.N. A finite-element model for piezoelectric composite laminates. *Smart Mater. Struct.* **1997**, *6*, 583–591. [CrossRef]
22. Sheikh, A.H.; Mukhopadhyay, M. Linear and nonlinear transient vibration analysis of stiffened plate structures. *Finite Elem. Anal. Des.* **2002**, *38*, 477–502. [CrossRef]
23. Mukhergee, A.; Joshi, S.P.; Ganguli, A. Active vibration control of piezolaminated stiffened plates. *Compos. Struct.* **2002**, *55*, 435–443. [CrossRef]